Draft version May 24, 2018
Typeset using LaTeX **preprint** style in AASTeX62

Spitzer Microlensing Parallax for OGLE-2017-BLG-0896 Reveals a Counter-Rotating Low-Mass Brown Dwarf

Yossi Shvartzvald,[1] Jennifer C. Yee,[2] Jan Skowron,[3] Chung-Uk Lee,[4,5] Andrzej Udalski,[3] Sebastiano Calchi Novati,[1] and Valerio Bozza[6,7]

—

Charles A. Beichman,[1] Geoffery Bryden,[8] Sean Carey,[1] B. Scott Gaudi,[9] Calen B. Henderson,[1] and Wei Zhu[10]
(*Spitzer* team)

Etienne Bachelet,[11] Greg Bolt,[12] Grant Christie,[13] Dan Maoz,[14] Tim Natusch,[13,15] Richard W. Pogge,[9] Rachel A. Street,[11] Thiam-Guan Tan,[16] and Yiannis Tsapras[17]
(LCO and μFUN Follow-up Teams)

Paweł Pietrukowicz,[3] Igor Soszyński,[3] Michał K. Szymański,[3] Przemek Mróz,[3] Radoslaw Poleski,[3,9] Szymon Kozłowski,[3] Krzysztof Ulaczyk,[3] Michał Pawlak,[3] Krzysztof A. Rybicki,[3] and Patryk Iwanek[3]
(OGLE Collaboration)

Michael D. Albrow,[18] Sang-Mok Cha,[4,19] Sun-Ju Chung,[4,5] Andrew Gould,[4,20,9] Cheongho Han,[21] Kyu-Ha Hwang,[4] Youn Kil Jung,[2,4] Dong-Jin Kim,[4] Hyoun-Woo Kim,[4] Seung-Lee Kim,[4,5] Dong-Joo Lee,[4] Yongseok Lee,[4,19] Byeong-Gon Park,[4,5] Yoon-Hyun Ryu,[4] In-Gu Shin,[2] and Weicheng Zang[22,23]
(KMTNet Collaboration)

Martin Dominik,[24] Christiane Helling,[24] Markus Hundertmark,[17] Uffe G. Jørgensen,[25] Penelope Longa-Peña,[26] Stephen Lowry,[27] Sedighe Sajadian,[28] Martin J. Burgdorf,[29] Justyn Campbell-White,[27] Simona Ciceri,[30] Daniel F. Evans,[31] Yuri I. Fujii,[25,32,33] Tobias C. Hinse,[4] Sohrab Rahvar,[34] Markus Rabus,[35,36] Jesper Skottfelt,[37,25] Colin Snodgrass,[37] and John Southworth[31]
(MiNDSTEp Collaboration)

[1] *IPAC, Mail Code 100-22, Caltech, 1200 E. California Blvd., Pasadena, CA 91125, USA*
[2] *Harvard-Smithsonian Center for Astrophysics, 60 Garden St.,Cambridge, MA 02138, USA*
[3] *Warsaw University Observatory, Al. Ujazdowskie 4, 00-478 Warszawa, Poland*
[4] *Korea Astronomy and Space Science Institute, Daejon 34055, Republic of Korea*
[5] *Korea University of Science and Technology, 217 Gajeong-ro, Yuseong-gu, Daejeon 34113, Republic of Korea*
[6] *Dipartimento di Fisica "E.R. Caianiello", Università di Salerno, Via Giovanni Paolo II 132, 84084, Fisciano, Italy*
[7] *Istituto Nazionale di Fisica Nucleare, Sezione di Napoli, Napoli, Italy*
[8] *Jet Propulsion Laboratory, California Institute of Technology, 4800 Oak Grove Drive, Pasadena, CA 91109, USA*
[9] *Department of Astronomy, Ohio State University, 140 W. 18th Ave., Columbus, OH 43210, USA*
[10] *Canadian Institute for Theoretical Astrophysics, University of Toronto, 60 St George Street, Toronto, ON M5S 3H8, Canada*
[11] *Las Cumbres Observatory, 6740 Cortona Drive, suite 102, Goleta, CA 93117, USA*
[12] *Craigie, Western Australia, Australia*
[13] *Auckland Observatory, Auckland, New Zealand*

Corresponding author: Yossi Shvartzvald
yossishv@gmail.com

[14] *School of Physics and Astronomy, Tel-Aviv University, Tel-Aviv 6997801, Israel*
[15] *Institute for Radio Astronomy and Space Research (IRASR), AUT University, Auckland, New Zealand*
[16] *Perth Exoplanet Survey Telescope, Perth, Australia*
[17] *Astronomisches Rechen-Institut, Zentrum für Astronomie der Universität Heidelberg (ZAH), 69120 Heidelberg, Germany*
[18] *University of Canterbury, Department of Physics and Astronomy, Private Bag 4800, Christchurch 8020, New Zealand*
[19] *School of Space Research, Kyung Hee University, Yongin, Kyeonggi 17104, Republic of Korea*
[20] *Max-Planck-Institute for Astronomy, Königstuhl 17, 69117 Heidelberg, Germany*
[21] *Department of Physics, Chungbuk National University, Cheongju 28644, Republic of Korea*
[22] *Physics Department and Tsinghua Centre for Astrophysics, Tsinghua University, Beijing 100084, China*
[23] *Department of Physics, Zhejiang University, Hangzhou, 310058, China*
[24] *Centre for Exoplanet Science, SUPA, School of Physics & Astronomy, University of St Andrews, North Haugh, St Andrews KY16 9SS, UK*
[25] *Niels Bohr Institute & Centre for Star and Planet Formation, University of Copenhagen, Øster Voldgade 5, 1350 Copenhagen, Denmark*
[26] *Unidad de Astronomía, Facultad de Ciencias Básicas, Universidad de Antofagasta, Av. Angamos 601, Antofagasta, Chile*
[27] *Centre for Astrophysics & Planetary Science, The University of Kent, Canterbury CT2 7NH, UK*
[28] *Department of Physics, Isfahan University of Technology, Isfahan 84156-83111, Iran*
[29] *Universität Hamburg, Faculty of Mathematics, Informatics and Natural Sciences, Department of Earth Sciences, Meteorological Institute, Bundesstraße 55, 20146 Hamburg, Germany*
[30] *Department of Astronomy, Stockholm University, Alba Nova University Center, 106 91, Stockholm, Sweden*
[31] *Astrophysics Group, Keele University, Staffordshire, ST5 5BG, UK*
[32] *Institute for Advanced Research, Nagoya University, Furo-cho, Chikusa-ku, Nagoya, 464-8601, Japan*
[33] *Department of Physics, Nagoya University, Furo-cho, Chikusa-ku, Nagoya 464-8602, Japan*
[34] *Department of Physics, Sharif University of Technology, PO Box 11155-9161 Tehran, Iran*
[35] *Centro de Astroingeniería, Facultad de Física, Pontificia Universidad Católica de Chile, Av. Vicuña Mackenna 4860, Macul 7820436, Santiago, Chile*
[36] *Max Planck Institute for Astronomy, Königstuhl 17, 69117 Heidelberg, Germany*
[37] *School of Physical Sciences, Faculty of Science, Technology, Engineering and Mathematics, The Open University, Walton Hall, Milton Keynes, MK7 6AA, UK*

ABSTRACT

The kinematics of isolated brown dwarfs in the Galaxy, beyond the solar neighborhood, is virtually unknown. Microlensing has the potential to probe this hidden population, as it can measure both the mass and five of the six phase-space coordinates (all except the radial velocity) even of a dark isolated lens. However, the measurements of both the microlens parallax and finite-source effects are needed in order to recover the full information. Here, we combine *Spitzer* satellite parallax measurement with the ground-based light curve, which exhibits strong finite-source effects, of event OGLE-2017-BLG-0896. We find that the lens is a $\sim 19 M_J$ isolated brown dwarf. This is the lowest isolated-object mass measurement to date, only slightly above the common definition of a free-floating planet. The brown dwarf is located at $\sim$4 kpc toward the Galactic bulge, but with proper motion in the opposite direction of disk stars, possibly

moving in the Galactic plane. While it is possibly a halo brown dwarf, it might also represent a different, unknown population.

Keywords: gravitational lensing: micro — Galaxy: bulge

1. INTRODUCTION

The census, including kinematics, of luminous stars has been rapidly improving over the past decade and has just taken a further quantum leap with the publication of the Gaia DR2 data release (Gaia Collaboration et al. 2018). In general, it is usually supposed that low-mass brown dwarfs, which are essentially invisible beyond the immediate solar neighborhood, share the kinematics of "normal" stars. While there are no theoretical arguments against this hypothesis, neither is there any observational evidence in its favor.

Spitzer microlensing offers a unique opportunity to probe the kinematics of low-mass objects. From 2014-2018, *Spitzer* has been observing a total of nearly 1000 microlensing events toward the Galactic bulge (Gould et al. 2013, 2014, 2015a,b, 2016) with the aim of measuring their microlens parallax, $\boldsymbol{\pi}_{\rm E}$,

$$\boldsymbol{\pi}_{\rm E} = \frac{\pi_{\rm rel}}{\theta_{\rm E}} \frac{\boldsymbol{\mu}_{\rm rel}}{\mu_{\rm rel}}; \qquad \theta_{\rm E} = \sqrt{\kappa M \pi_{\rm rel}}; \qquad \kappa \equiv \frac{4G}{c^2 {\rm AU}} \simeq 8.14 \frac{\rm mas}{M_\odot}, \tag{1}$$

where $(\pi_{\rm rel}, \boldsymbol{\mu}_{\rm rel})$ are the lens-source relative (parallax, proper motion) and M is the mass of the lens. For special cases in which the angular Einstein radius $\theta_{\rm E}$ is measured, the *Spitzer* measurement of $\boldsymbol{\pi}_{\rm E}$ then yields M and $(\pi_{\rm rel}, \boldsymbol{\mu}_{\rm rel})$.

$$M = \frac{\theta_{\rm E}}{\kappa \pi_{\rm E}}; \qquad \pi_{\rm rel} = \theta_{\rm E} \pi_{\rm E}; \quad \boldsymbol{\mu}_{\rm rel} = \frac{\theta_{\rm E}}{t_{\rm E}} \frac{\boldsymbol{\pi}_{\rm E}}{\pi_{\rm E}}, \tag{2}$$

where $t_{\rm E}$ is the Einstein timescale of the microlensing event. Then, if the source parallax π_s and proper motion $\boldsymbol{\mu}_s$ are independently measured, one can infer five of the six phase-space coordinates of the lens (even if it is dark), i.e., its position on the sky and

$$\pi_l = \pi_{\rm rel} + \pi_s; \qquad \boldsymbol{\mu}_l = \boldsymbol{\mu}_{\rm rel} + \boldsymbol{\mu}_s. \tag{3}$$

The key additional step (assuming that $\boldsymbol{\pi}_{\rm E}$ is measured) is to measure $\theta_{\rm E}$. For luminous lenses, this can in principle be done by waiting until the lens is well separated from the source, when they can be separately imaged. In this case, their observed separation $\Delta\boldsymbol{\theta}$ immediately gives $\boldsymbol{\mu}_{\rm rel} = \Delta\boldsymbol{\theta}/\Delta t$, where Δt is the elapsed time since the event. To date such measurements are relatively rare (Alcock et al. 2001; Batista et al. 2015; Bennett et al. 2015) because one must wait more than 10 years for typical events to separate, but with next generation ("30m") telescopes, they are likely to become routine.

However, for dark lenses, there are only two known methods to measure $\theta_{\rm E}$: astrometric microlensing (Miyamoto & Yoshii 1995; Hog et al. 1995; Walker 1995) and finite-source effects (Gould 1994a). Astrometric microlensing is not generally well-suited to low-mass lenses because their $\theta_{\rm E}$ are small. Moreover, while it is a potentially powerful approach for high-mass lenses (e.g., Gould & Yee 2014), it can only be applied to a tiny handful of events with current instruments. This implies that measuring finite-source effects (together with microlens parallaxes) is presently the only viable method to acquire a sample of low-mass dark lenses with measured kinematics.

Spitzer microlensing is providing a steady stream of isolated-object mass measurements that is strongly biased toward both low-mass lenses and bright sources. The latter enable relatively easy measurements of $\boldsymbol{\mu}_s$, while π_s is reasonably well known for essentially all microlensing events. With these quantities one can apply Equations (2) and (3) to obtain the lens kinematics.

Finite-source effects (i.e., deviations in the light curve relative to the predictions for a point source), occur when a source transits a caustic in the magnification structure (or comes very close to a cusp). This occurs relatively frequently for binary and planetary events because the binary caustic structures are relatively large while the events are usually recognized as planetary in nature because the source passes over or very near a caustic. However, for isolated lenses, the "caustic" consists of a single point, i.e., directly behind the lens itself. Thus, the probability of such a caustic passage (given that there is a microlensing event) is

$$P = \rho \equiv \frac{\theta_*}{\theta_{\rm E}}, \tag{4}$$

where θ_* is the source angular size. This simple equation has two very important implications. First, it means that the rate $\Gamma_{\rm FS} = \rho\Gamma_{\mu\rm lens}$ of events with finite source effects does not depend on the mass of some class of lenses, but only on their number density n (Gould & Yee 2012). That is, while the microlensing rate $\Gamma_{\mu\rm lens} \propto n\mu_{\rm rel}\theta_{\rm E}$ increases with mass as $\Gamma_{\mu\rm lens} \propto M^{1/2}$, the finite-source rate

$$\Gamma_{\rm FS} = \rho\Gamma_{\mu\rm lens} \propto n\mu_{\rm rel}\theta_* \tag{5}$$

does not. Thus, there is a strong bias toward the more common low-mass objects. Second, because (from Equation (5)) $\Gamma_{\rm FS} \propto \theta_*$, finite-source effects are strongly biased toward large (hence, bright) stars.

There are four published isolated-object mass measurements from *Spitzer* microlensing in 2015 and 2016 (Zhu et al. 2016; Chung et al. 2017; Shin et al. 2018), and four more that we have identified from *Spitzer* microlensing in 2017. These have masses in ascending order, $M = (19, 45, 58^\dagger, 80, 88, 235^\dagger, 520, 570^\dagger) M_{\rm jup}$, which illustrates the strong bias toward low mass objects. Here the "†" symbol indicates preliminary estimates for not-yet-published events. Their source radii are $\theta_* = (1.4, 5.7, 5.8, 6.0^\dagger, 6.3, 6.8^\dagger, 7.8, 33.7^\dagger)\mu$as, which should be compared to $\theta_* \sim 0.5\mu$as for typical microlensing events.

Here we present the first of the 2017 *Spitzer* isolated-object microlensing mass measurements, OGLE-2017-BLG-0896L. As we will report, it has $M \simeq 19\,M_J$, making it the lowest-mass object of the sample of eight that have been measured to date. Indeed, this was the initial focus of our interest. However, in the course of checking our results, we noted that the values of $(\pi_{\rm rel}, \boldsymbol{\mu}_{\rm rel})$, which are automatically returned as part of the mass derivation, pointed to a possible conflict with the known kinematic characteristics of the major populations of the Galaxy. Because this discrepancy could be resolved if the source had mildly unusual characteristics, we undertook the additional step of measuring the source proper motion $\boldsymbol{\mu}_s$. Contrary to our expectation, this measurement made the conflict substantially worse. Of course, one cannot draw very strong conclusions from a single unusual object. However, as we note, there are at least some indications that this object may be a member of previously unrecognized population.

2. OBSERVATIONS

OGLE-2017-BLG-0896 is at (RA,Dec) = (17:39:30.98,−27:17:51.1) corresponding to $(l, b) = (0.69, 2.01)$. It was discovered and announced as a probable microlensing event by the OGLE Early

Warning System (Udalski et al. 1994; Udalski 2003) at UT 20:23 on 25 May 2017. The event lies in OGLE field BLG675 (Udalski et al. 2015), for which OGLE observations were at a cadence of 1–3 obs/night using their 1.3m telescope at Las Campanas, Chile.

The Korea Microlensing Telescope Network (KMTNet, Kim et al. 2016) observed this field from its three 1.6m telescopes at CTIO (Chile, KMTC), SAAO (South Africa, KMTS) and SSO (Australia, KMTA), in its field BLG15 with a cadence of 1 obs/hr. It is designated SAO15N0405.007056 in the KMTNet catalog. We exclude for the fit the KMTNet data over the peak of the event, at HJD'$\equiv$ HJD$-$2450000=[7910–7912], as the event got too bright and thus the photometry is affected by nonlinearity.

The great majority of these survey observations were carried out in the I band with occasional V-band observations made solely to determine source colors. All reductions for the light curve analysis were conducted using variants of difference image analysis (DIA, Alard & Lupton 1998), specifically Wozniak (2000) and Albrow et al. (2009).

OGLE-2017-BLG-0896 was announced as a *Spitzer* target at UT 09:21 on 5 June because it was recognized as a relatively high-magnification event $A_{\rm max} \gtrsim 20$ and so with good (Gould & Loeb 1992; Abe et al. 2013) or possibly excellent (Griest & Safizadeh 1998) sensitivity to planets. The *Spitzer* observations themselves could not begin until 17 days later, when the event entered the sun-angle window, which was coincidentally the first epoch of planned observations, beginning UT 15:46 June 22. The *Spitzer* data were reduced using the Calchi Novati et al. (2015a) algorithm for crowded-field photometry.

The *Spitzer* team alerted the event as high-magnification and mobilized intensive follow-up observations, with the aim of detecting and characterizing any planetary signatures. Follow-up observations were carried out using four of the Las Cumbres Observatory (LCO) global network of telescopes in Chile, South Africa, and Australia, with the SDSS-i' filter. The Microlensing Follow Up Network (μFUN) followed the event using the 1.3m SMARTS telescope at CTIO (CT13) with $V/I/H$-bands, the 0.4m telescope at Auckland Observatory (AO) with R-band, the 0.3m Perth Exoplanet Survey Telescope (PEST) at Perth, Western Australia, and the 0.25m telescope at Craigie, Western Australia (unfiltered). PEST data were excluded from the analysis due to systematics of unknown origin. The MiNDSTEp team followed the event using the Danish 1.54-m telescope hosted at ESO's La Silla observatory in Chile, with a simultaneous two-color instrument (wide visible and red; See Figure 1 of Evans et al. 2016) providing Lucky Imaging photometry (Skottfelt et al. 2015). For the analysis of the event we use only the Danish red-band data. LCO and AO data were reduced using pySIS (Albrow et al. 2009), CT13 and Craigie data were reduced using DoPhot (Schechter et al. 1993), and Danish data were reduced using a modified version of DanDIA (Bramich et al. 2008).

While no planetary anomalies were detected, the follow-up observations were crucial in order to model the finite-source effects that are clearly shown at the peak of the event (see Figure 1) because the KMTNet data over the peak were affected by nonlinearity and OGLE cadence was not sufficient for the characterization.

3. LIGHT CURVE ANALYSIS

3.1. *Ground data only*

The light curve, as seen from Earth, is of a symmetric high-magnification event with clear deviation from a point source microlensing (Figure 1). These features rule out any reasonable binary lens since

no anomaly/asymmetry associated with a central caustic is detected. The *Spitzer* data cover only the falling tail of the event, thus not constraining the finite-source size. Therefore, we start by modeling the ground-based data alone.

We fit the ground-based light curve using six parameters to describe the geometry of finite-source point-lens (FSPL) microlensing as well as two flux parameters for each dataset, $f_{s,i}, f_{b,i}$ (for the source and possible blend). The geometric parameters are the Paczyński parameters, $(t_0, u_0, t_{\rm E})$ (Paczyński 1986), the scaled angular source size $\rho = \theta_*/\theta_{\rm E}$, and the limb-darkening coefficients Γ_I and $\Gamma_{\rm Danish}$ (we use a specific coefficient for the Danish data because of the non-standard filter). We adopt a limb-darkened brightness profile for the source star of the form

$$S_\lambda(\theta) = \bar{S}_\lambda \left[1 - \Gamma_\lambda \left(1 - \frac{3}{2}\cos\theta\right)\right], \tag{6}$$

where $\bar{S}_\lambda \equiv f_{s,\lambda}/(\pi\theta_\star^2)$ is the mean surface brightness of the source, θ is the angle between the normal to the surface of the source star and the line of sight, $f_{s,\lambda}$ is the total source flux and Γ_λ is the limb-darkening coefficient at wavelength λ, respectively (An et al. 2002). The limb-darkening coefficients are usually estimated using the source intrinsic properties, which are interpreted from the offset between its observed color and magnitude and the red clump centroid. For this interpretation one assumes that the source is at a similar distance as the clump (i.e., in the bulge). In the case of OGLE-2017-BLG-0896L, the dense coverage during the finite-source effects allows us to well constrain the limb-darkening coefficient, Γ_I, thus enabling us to verify that indeed the source is a bulge star (see Section 4). We use Γ_I and $\Gamma_{\rm Danish}$ as free fit parameters, as most of our observations over the peak are with these bands[1]. For AO (R-band) and Craigie (unfiltered) data, we estimate the limb-darkening coefficient as $(\Gamma_I+\Gamma_V)/2$, where $\Gamma_V = 0.754$ was determined from Claret & Bloemen (2011) based on the characterized source properties (Section 4). The V- (OGLE/KMTNet/CT13) and H-band (CT13) data are used only to derive the source color, and thus do not require limb-darkening coefficients.

3.2. *Satellite parallax degeneracy*

In order to include the *Spitzer* data we add two microlensing parallax parameters, $\pi_{\rm E,N}, \pi_{\rm E,E}$, aligned with the equatorial north and east directions. Generally, this can introduce the well known four-fold satellite parallax degeneracy (Refsdal 1966; Gould 1994b). However, because $|u_{0,ground}| \ll 1$ the magnitude $|\boldsymbol{\pi}_{\rm E}|$ is nearly the same for all solutions (Gould & Yee 2012), and thus the mass and distance of the lensing system are similar. A two-fold degeneracy in the direction of the relative proper motion between the source and the lens persists.

Because *Spitzer* data covered only the falling part of the event and in addition did not fully cover the baseline of the event (see inset of Figure 1), they cannot set strong constraints on $\boldsymbol{\pi}_{\rm E}$ by themselves. However, by applying a constraint on the *Spitzer* source flux based on color-color relations, the parallax measurement can be significantly improved (e.g., Calchi Novati et al. 2015b). We derive two color-color relations for OGLE-2017-BLG-0896: a VIL relation (using KMTNet data) and an IHL relation (using CT13 data), as detailed in Section 4.1. The constraints on *Spitzer* source flux using each of the relations, and consequently the derived parallax values, are in good agreement with

[1] We use Γ_I also for LCO SDSS-i' data.

each other ($< 1\sigma$). We adopt the VIL relation for the final results, because the CT13 data might be subject to low-level chromatic effects.

Table 1 gives the best-fit parameters and their uncertainties for the four-fold degenerate solutions ($\Delta\chi^2 < 4$). The microlensing parallax components are well constrained, with $\sim 4\%$ and $\sim 8\%$ uncertainties on $\pi_{\rm E,N}$ and $\pi_{\rm E,E}$, respectively. These are significantly better than the results without the constraint on *Spitzer* flux, which have $15-30\%$ uncertainties on the parallax components. It is important to note, however, that the median values are similar. In particular, $\pi_{\rm E,E} < 0$ at the 3σ level even without the color constraint, which is both surprising and interesting as we discuss below in Section 5.

3.2.1. *Negative Spitzer blending*

The *Spitzer* blend flux is constrained to be negative when using the color-color relations, $f_{b,Spitzer} = -4.4 \pm 1.2$. While negative blending is known to sometimes be present in ground-based microlensing light curves (e.g., Jiang et al. 2004), its origin in these cases is not always clear. However, for *Spitzer* photometry in crowded fields using the Calchi Novati et al. (2015a) algorithm, the cause for possible artificial negative blending is well understood. As detailed in Calchi Novati et al. (2015a), an input catalog of sources is used to retrieve the *Spitzer* photometry around the event. The catalog is constructed from optical survey data (KMTNet data in the case of OGLE-2017-BLG-0896), which have better resolution and depth than the *Spitzer* image. Any source that is not in the catalog (i.e., unresolved faint stars) will be absorbed in the global background flux, which effectively is subtracted from the source flux, thus resulting as an artificial negative blending. Naturally, this will be more significant in cases for which no real underlying blend in the source position is detected, like in our case ($f_{b,ogle} = 0.028 \pm 0.009$, corresponding to 5σ limit of $I_b > 20.8$).

Examining the optical image around the event and comparing it to nearby ($< 15''$) isolated regions, we find an excess of flux due to unresolved stars. The *Spitzer* flux in the isolated regions is significantly lower than the background estimation at the source position. After taking into account *Spitzer* point-response function, this difference correspond to $\sim$5 flux units of artificial negative blending, which therefore fully explains the negative blend found for *Spitzer*.

4. SOURCE STAR

4.1. *CMD analysis and color-color relations*

The source photometric properties (color and magnitude) are important for several reasons. First, the source intrinsic properties yield its angular size, θ_*, which is needed to derive $\theta_{\rm E}$ and the physical properties of the lensing system (Equation (2)). Second, they are used to estimate the limb-darkening coefficients, or alternatively (as in our case) can be compared to the fitted coefficients to verify the estimate of the distance to the source. Lastly, instrumental color-color relations can help constrain the source flux in a third band based on one measured color (e.g., the *Spitzer* L-band source flux based on an optical color).

Figure 2 shows the KMTC V/I instrumental color-magnitude diagram (CMD) constructed from sources within $< 2'$ of the event. We measure the instrumental centroid of the red clump $(V-I, I)_{\rm cl,kmt} = (2.71, 14.18)$ and compare it to the intrinsic centroid of $(V-I, I)_{\rm cl,0} = (1.06, 14.41)$ (Bensby et al. 2013; Nataf et al. 2013). We determine the instrumental source color from regression of V versus I flux as the source magnification changes (Gould et al. 2010), and find $(V-I)_{s,\rm kmt} = 2.91 \pm 0.03$. The source instrumental magnitude, as inferred from the microlensing model, is $I_{s,\rm kmt} =$

14.72 ± 0.01. Assuming that the source lies behind the same dust column as the red clump, its intrinsic properties are $(V-I, I)_{s,0} = (1.26, 14.95) \pm (0.06, 0.04)$, accounting also for the red clump instrumental and intrinsic uncertainties. Using standard color-color relations (Bessell & Brett 1988) and the relation between angular source size and surface brightness (Kervella et al. 2004), we find $\theta_* = 5.71 \pm 0.29\,\mu$as.

The source position on the CMD, under the assumption it is a bulge star, suggests a K2.5 III spectral type with $T_{\rm eff} \approx 4300$ and $\log(g) \approx 2.2$. The corresponding linear limb-darkening coefficients (Claret & Bloemen 2011) are $\Gamma_I = 0.519 \pm 0.015$ and $\Gamma_V = 0.754 \pm 0.021$, where the uncertainties account for a range of possible metallicities and microturbulence velocities. The limb-darkening coefficient Γ_I derived from the fit, for all four degenerate solutions (see Table 1), is within excellent agreement of the estimate based on the source spectral type. This confirms the assumption of a bulge source with similar distance as the red clump.

We extract *Spitzer* photometry for red giant branch stars ($13.7 < I_{\rm KMT} < 14.7\,; 2.45 < (V-I)_{\rm KMT} < 2.95$), which are a good representation of the bulge giant population, and derive an instrumental VIL color-color relation (Calchi Novati et al. 2015a). Applying the relation to the measured $(V-I)_{s,\rm KMT}$, we find $(I_{\rm KMT} - L_{Spitzer})_s = 0.31 \pm 0.05$. Using this constraint in the microlensing model gives $f_{s,Spitzer} = 27.2 \pm 1.2$. For consistency, we also derive the instrumental IHL relation using CT13 data. Applying it to $(I-H)_{s,\rm CT13} = 0.53 \pm 0.02$ (derived from regression), we find $(I_{\rm CT13} - L_{Spitzer})_s = 4.45 \pm 0.03$. This gives $f_{s,Spitzer} = 27.0 \pm 0.7$, in excellent agreement with the constraint using the VIL relation. We note that almost all CT13 data (except 3 baseline epochs) were taken during the finite-source effects, and thus they might exhibit low-level chromatic effects.

4.2. *Source proper motion*

The lens proper motion can be derived from the relative-proper motion and the source proper motion (Equation (3)). The source star of OGLE-2017-BLG-0896 is bright, isolated and with negligible blending, thus permitting a good measurement of its proper motion (unlike most microlensing sources, which are faint and blended). We construct a deep OGLE CMD from a $6.5' \times 6.5'$ region centered around the event, and identify 1527 red clump bulge stars and 730 foreground disk stars. We then use 387 good seeing (<1.35") OGLE epochs from HJD'=5385–8030 to measure the vector proper motion of each star, with typical uncertainty of 0.45 mas yr^{-1} for clump stars. We find that the source proper motion is $\mu_s(N,E) = (-5.10, -3.15) \pm (0.46, 0.44)$mas yr^{-1} relative to the frame set by the clump giants. Figure 3 shows the source proper motion along with the proper motion distributions of bulge and disk stars. The position of the source on this diagram further supports it being part of the bulge population.

5. THE LENS - COUNTER-ROTATING BROWN DWARF

The Einstein angular radius is determined by combining ρ from the model and θ_* from the CMD,

$$\theta_{\rm E} = 0.140 \pm 0.007\,{\rm mas}. \tag{7}$$

Combining this with the four-degenerate parallax solutions from the microlensing model (Equation (2)) yields a low-mass BD of $M \simeq 19\,M_J$, with minor differences within 1-2σ between the models (See Table 2). The distance to the BD (Equation (3)) is $D_L \simeq 4$ kpc, where we assumed $D_S = 8.3$ kpc, which is appropriate for a bulge source toward the event direction.

The geocentric relative proper motion (Equation (2)) is $\mu_{\rm rel,geo} = 3.42 \pm 0.18\,{\rm mas\,yr^{-1}}$, with either a North-West or a South-West direction as inferred from the parallax components. These already suggest some tension with a disk lens (as would seem to be inferred by D_L). In principle, this tension could be resolved if the source had significant North-East proper motion. However, as we found in Section 4.2, the source is actually moving in the opposite direction. Accounting for Earth's projected velocity at the peak of the event, $V_{\oplus,\perp}(N,E) = (-0.68, 28.9)\,{\rm km\,s^{-1}}$, the two degenerate solutions for the BD heliocentric proper motion relative to the frame set by the bulge clump giants are (see Figure 3),

$$\mu_{l,\rm hel}(N,E) = \boldsymbol{\mu}_s + (\boldsymbol{\mu}_{\rm rel,geo} + \pi_{\rm rel}\boldsymbol{V}_{\oplus,\perp}) = \begin{cases} (-7.8,-4.4) \pm (0.5,0.5)\,{\rm mas\,yr^{-1}} \\ \text{or} \\ (-2.5,-4.7) \pm (0.5,0.5)\,{\rm mas\,yr^{-1}} \end{cases} \tag{8}$$

In order to find the lens projected velocity, we first note that

$$\boldsymbol{\mu}_{l,\rm hel} = \boldsymbol{\mu}_s + \boldsymbol{\mu}_{\rm rel,hel} = \left(\frac{\boldsymbol{V}_s - \boldsymbol{V}_\odot}{D_s} - \frac{\boldsymbol{V}_{\rm cl} - \boldsymbol{V}_\odot}{D_{\rm cl}}\right) + \left(\frac{\boldsymbol{V}_l - \boldsymbol{V}_\odot}{D_l} - \frac{\boldsymbol{V}_s - \boldsymbol{V}_\odot}{D_s}\right) \tag{9}$$

where $\boldsymbol{V}_{\rm cl}$ and $D_{\rm cl}$ are, respectively, the mean velocity and distance of the clump stars that set the proper-motion reference frame. Because the event is at $l \approx 0$, we adopt $V_{\rm cl}(l,b) = (0,0)\,{\rm km\,s^{-1}}$ and $D_{\rm cl} = 8.3$ kpc. The Sun's velocity consists of peculiar velocity, $V_{\odot,\rm pec}(l,b) = (12,7)\,{\rm km\,s^{-1}}$, and the disk circular velocity, $V_{\rm rot}(l,b) = (220,0)\,{\rm km\,s^{-1}}$. Therefore, the two degenerate solutions for the lens peculiar velocity relative to the mean motion disk stars in its neighborhood are

$$\begin{aligned} V_{l,\rm pec}(l,b) = \boldsymbol{V}_l - \boldsymbol{V}_{\rm rot} &= D_l\boldsymbol{\mu}_{l,\rm hel} - \boldsymbol{V}_{\rm rot}\left(\frac{D_l}{D_{\rm cl}}\right) + \boldsymbol{V}_{\odot,\rm pec}\left(1 - \frac{D_l}{D_{\rm cl}}\right) \\ &= \begin{cases} (-268,-7) \pm (10,9)\,{\rm km\,s^{-1}} \\ \text{or} \\ (-199,51) \pm (10,10)\,{\rm km\,s^{-1}} \end{cases} \end{aligned} \tag{10}$$

These should be compared to the standard deviations for the disk velocities of $\sigma_{\rm rot}(l,b) = (30,20)\,{\rm km\,s^{-1}}$. Thus, in both cases the BD is significantly counter-rotating relative to the disk-stars' motion. Interestingly, one of these solutions is consistent, within small error bars, with perfectly planar counter-rotation. The other solution has considerable out-of-plane motion.

6. DISCUSSION

We have presented the discovery of an $\sim 19 M_J$ isolated BD, the lowest-mass isolated object ever measured. The BD is located at $D_L \simeq 4$ kpc toward the Galactic bulge, but it is counter-rotating with respect to the kinematics of "normal" disk stars at this location. This is not the first example of a low-mass object with unusual kinematics. OGLE-2016-BLG-1195L (Shvartzvald et al. 2017) is a planetary system at $D_L \simeq 4$ kpc with an Earth-mass planet orbiting an ultracool dwarf ($\sim 0.08 M_\odot$), with significant West relative proper motion, $\mu_{\rm hel,E} \simeq -7.5\,{\rm mas\,yr^{-1}}$, although in that case the source proper motion was not measured and thus a fast moving source ($\sim 360\,{\rm km\,s^{-1}}$ relative to the bulge) is also possible. OGLE-2016-BLG-0864L (Chung et al. 2018, in preparation) is a BD-BD binary system at $D_L \simeq 3$ kpc, with relative proper motion suggesting the system is counter-rotating with

respect to the disk motion (though, again, the source proper motion was not measured). In addition, while most local BDs have similar kinematics as stars (e.g., Faherty et al. 2009), there is a growing sample of local BDs (Zhang et al. 2017) associated with kinematics of halo stars, including even a counter-rotating BD (Cushing et al. 2009).

The combined measurements of the satellite microlens parallax with *Spitzer* and the detection of finite-source effects, enabled the full characterization of the BD properties. Microlensing is the only technique that can characterize the kinematics of low-mass dark objects throughout the Galaxy. This method can also be extended to free-floating planets (Henderson & Shvartzvald 2016; Gould 2016). A possible explanation of the kinematics of OGLE-2017-BLG-0896L is that it is a halo BD. Alternatively, it might suggest, along with the other examples mentioned above, the existence of a counter-rotating population of low-mass objects. The selection criteria of *Spitzer* events (Yee et al. 2015), with the 3-10 day lag before event selection and the beginning of *Spitzer* observations, is favoring the detection of these BDs, which have longer timescales than expected by "normal" disk star kinematics (e.g. OGLE-2017-BLG-0896L, OGLE-2016-BLG-1195L). In addition, counter-rotating lenses will peak later as seen from *Spitzer* than from Earth, thus increasing the chances for parallax measurement.

We thank D. Kirkpatrick for fruitful discussions about BDs. Work by YKJ, and AG were supported by AST-1516842 from the US NSF. IGS, and AG were supported by JPL grant 1500811. Work by C. Han was supported by the grant (2017R1A4A1015178) of National Research Foundation of Korea. This work is based (in part) on observations made with the *Spitzer* Space Telescope, which is operated by the Jet Propulsion Laboratory, California Institute of Technology under a contract with NASA. Support for this work was provided by NASA through an award issued by JPL/Caltech. This work was partially supported by NASA contract NNG16PJ32C. The OGLE project has received funding from the National Science Centre, Poland, grant MAESTRO 2014/14/A/ST9/00121 to AU. This research has made use of the KMTNet system operated by the Korea Astronomy and Space Science Institute (KASI) and the data were obtained at three host sites of CTIO in Chile, SAAO in South Africa, and SSO in Australia. Work by SR and SS was supported by INSF-95843339. PL-P was supported by MINEDUC-UA project, code ANT 1656. The research has made use of data obtained at the Danish 1.54m telescope at ESOs La Silla Observatory.

REFERENCES

Abe, F., Airey, C., Barnard, E., et al. 2013, MNRAS, 431, 2975, doi: 10.1093/mnras/stt318

Alard, C., & Lupton, R. H. 1998, ApJ, 503, 325, doi: 10.1086/305984

Albrow, M. D., Horne, K., Bramich, D. M., et al. 2009, MNRAS, 397, 2099, doi: 10.1111/j.1365-2966.2009.15098.x

Alcock, C., Allsman, R. A., Alves, D. R., et al. 2001, Nature, 414, 617, doi: 10.1038/414617a

An, J. H., Albrow, M. D., Beaulieu, J.-P., et al. 2002, ApJ, 572, 521, doi: 10.1086/340191

Batista, V., Beaulieu, J.-P., Bennett, D. P., et al. 2015, ApJ, 808, 170, doi: 10.1088/0004-637X/808/2/170

Bennett, D. P., Bhattacharya, A., Anderson, J., et al. 2015, ApJ, 808, 169, doi: 10.1088/0004-637X/808/2/169

Bensby, T., Yee, J. C., Feltzing, S., et al. 2013, A&A, 549, A147, doi: 10.1051/0004-6361/201220678

Bessell, M. S., & Brett, J. M. 1988, PASP, 100, 1134, doi: 10.1086/132281

Bramich, D. M., Vidrih, S., Wyrzykowski, L., et al. 2008, MNRAS, 386, 887, doi: 10.1111/j.1365-2966.2008.13053.x
Calchi Novati, S., Gould, A., Yee, J. C., et al. 2015a, ApJ, 814, 92, doi: 10.1088/0004-637X/814/2/92
Calchi Novati, S., Gould, A., Udalski, A., et al. 2015b, ApJ, 804, 20, doi: 10.1088/0004-637X/804/1/20
Chung, S.-J., Zhu, W., Udalski, A., et al. 2017, ApJ, 838, 154, doi: 10.3847/1538-4357/aa67fa
Claret, A., & Bloemen, S. 2011, A&A, 529, A75, doi: 10.1051/0004-6361/201116451
Cushing, M. C., Looper, D., Burgasser, A. J., et al. 2009, ApJ, 696, 986, doi: 10.1088/0004-637X/696/1/986
Evans, D. F., Southworth, J., Maxted, P. F. L., et al. 2016, A&A, 589, A58, doi: 10.1051/0004-6361/201527970
Faherty, J. K., Burgasser, A. J., Cruz, K. L., et al. 2009, AJ, 137, 1, doi: 10.1088/0004-6256/137/1/1
Gaia Collaboration, Brown, A. G. A., Vallenari, A., et al. 2018, ArXiv e-prints. https://arxiv.org/abs/1804.09365
Gould, A. 1994a, ApJL, 421, L71, doi: 10.1086/187190
—. 1994b, ApJL, 421, L75, doi: 10.1086/187191
—. 2016, Journal of Korean Astronomical Society, 49, 123, doi: 10.5303/JKAS.2016.49.4.123
Gould, A., Carey, S., & Yee, J. 2013, Spitzer Microlens Planets and Parallaxes, Spitzer Proposal
—. 2014, Galactic Distribution of Planets from Spitzer Microlens Parallaxes, Spitzer Proposal
—. 2016, Galactic Distribution of Planets Spitzer Microlens Parallaxes, Spitzer Proposal
Gould, A., Dong, S., Bennett, D. P., et al. 2010, ApJ, 710, 1800, doi: 10.1088/0004-637X/710/2/1800
Gould, A., & Loeb, A. 1992, ApJ, 396, 104, doi: 10.1086/171700
Gould, A., Yee, J., & Carey, S. 2015a, Galactic Distribution of Planets From High-Magnification Microlensing Events, Spitzer Proposal
—. 2015b, Degeneracy Breaking for K2 Microlens Parallaxes, Spitzer Proposal
Gould, A., & Yee, J. C. 2012, ApJL, 755, L17, doi: 10.1088/2041-8205/755/1/L17
—. 2014, ApJ, 784, 64, doi: 10.1088/0004-637X/784/1/64
Griest, K., & Safizadeh, N. 1998, ApJ, 500, 37, doi: 10.1086/305729
Henderson, C. B., & Shvartzvald, Y. 2016, AJ, 152, 96, doi: 10.3847/0004-6256/152/4/96
Hog, E., Novikov, I. D., & Polnarev, A. G. 1995, A&A, 294, 287
Jiang, G., DePoy, D. L., Gal-Yam, A., et al. 2004, ApJ, 617, 1307, doi: 10.1086/425678
Kervella, P., Thévenin, F., Di Folco, E., & Ségransan, D. 2004, A&A, 426, 297, doi: 10.1051/0004-6361:20035930
Kim, S.-L., Lee, C.-U., Park, B.-G., et al. 2016, Journal of Korean Astronomical Society, 49, 37, doi: 10.5303/JKAS.2016.49.1.037
Miyamoto, M., & Yoshii, Y. 1995, AJ, 110, 1427, doi: 10.1086/117616
Nataf, D. M., Gould, A., Fouqué, P., et al. 2013, ApJ, 769, 88, doi: 10.1088/0004-637X/769/2/88
Paczyński, B. 1986, ApJ, 304, 1, doi: 10.1086/164140
Refsdal, S. 1966, MNRAS, 134, 315, doi: 10.1093/mnras/134.3.315
Schechter, P. L., Mateo, M., & Saha, A. 1993, PASP, 105, 1342, doi: 10.1086/133316
Shin, I.-G., Udalski, A., Yee, J. C., et al. 2018, AJ submitted, arXiv:1801.00169. https://arxiv.org/abs/1801.00169
Shvartzvald, Y., Yee, J. C., Calchi Novati, S., et al. 2017, ApJL, 840, L3, doi: 10.3847/2041-8213/aa6d09
Skottfelt, J., Bramich, D. M., Hundertmark, M., et al. 2015, A&A, 574, A54, doi: 10.1051/0004-6361/201425260
Udalski, A. 2003, AcA, 53, 291
Udalski, A., Szymanski, M., Kaluzny, J., et al. 1994, AcA, 44, 227
Udalski, A., Szymański, M. K., & Szymański, G. 2015, AcA, 65, 1. https://arxiv.org/abs/1504.05966
Walker, M. A. 1995, ApJ, 453, 37, doi: 10.1086/176367
Wozniak, P. R. 2000, AcA, 50, 421
Yee, J. C., Gould, A., Beichman, C., et al. 2015, ApJ, 810, 155, doi: 10.1088/0004-637X/810/2/155
Zhang, Z. H., Pinfield, D. J., Gálvez-Ortiz, M. C., et al. 2017, MNRAS, 464, 3040, doi: 10.1093/mnras/stw2438

Zhu, W., Calchi Novati, S., Gould, A., et al. 2016, ApJ, 825, 60, doi: 10.3847/0004-637X/825/1/60

Table 1. Microlensing model

	++	+−	−+	−−
χ^2	4126.8	4130.1	4127.0	4130.1
t_0 [HJD']	7911.05582(68)	7911.05601(68)	7911.05578(68)	7911.05601(68)
u_0	0.0039(11)	0.0037(12)	-0.0038(11)	-0.0037(12)
$t_{\rm E}$ [d]	14.883(93)	14.896(93)	14.885(93)	14.896(93)
ρ	0.04092(31)	0.04085(30)	0.04091(30)	0.04085(31)
Γ_I	0.525(13)	0.520(13)	0.523(13)	0.522(13)
$\Gamma_{\rm Danish}$	0.454(23)	0.450(23)	0.453(23)	0.450(23)
π_{EN}	-0.779(28)	0.662(29)	-0.771(28)	0.669(29)
π_{EE}	-0.615(46)	-0.587(46)	-0.613(46)	-0.589(46)

Table 2. Physical properties

	++	+−	−+	−−
$\theta_{\rm E}$ [mas]	0.1395(72)	0.1398(72)	0.1396(72)	0.1398(72)
M $[M_J]$	18.1(1.0)	20.3(1.2)	18.2(1.0)	20.2(1.1)
D_L [kpc]	3.86(11)	4.10(12)	3.88(11)	4.08(12)
$\mu_{\rm rel,geo}$ [mas yr^{-1}]	3.42(18)	3.43(18)	3.42(18)	3.43(18)
$\mu_{l,\rm hel}(N)$ [mas yr^{-1}]	-7.81(49)	-2.55(50)	-7.80(49)	-2.54(50)
$\mu_{l,\rm hel}(E)$ [mas yr^{-1}]	-4.43(48)	-4.67(49)	-4.44(48)	-4.65(49)
$v_{l,\rm pec}(l)$ [km s^{-1}]	-267(10)	-199(10)	-268(10)	-198(10)
$v_{l,\rm pec}(b)$ [km s^{-1}]	-7(9)	51(10)	-7(9)	50(10)

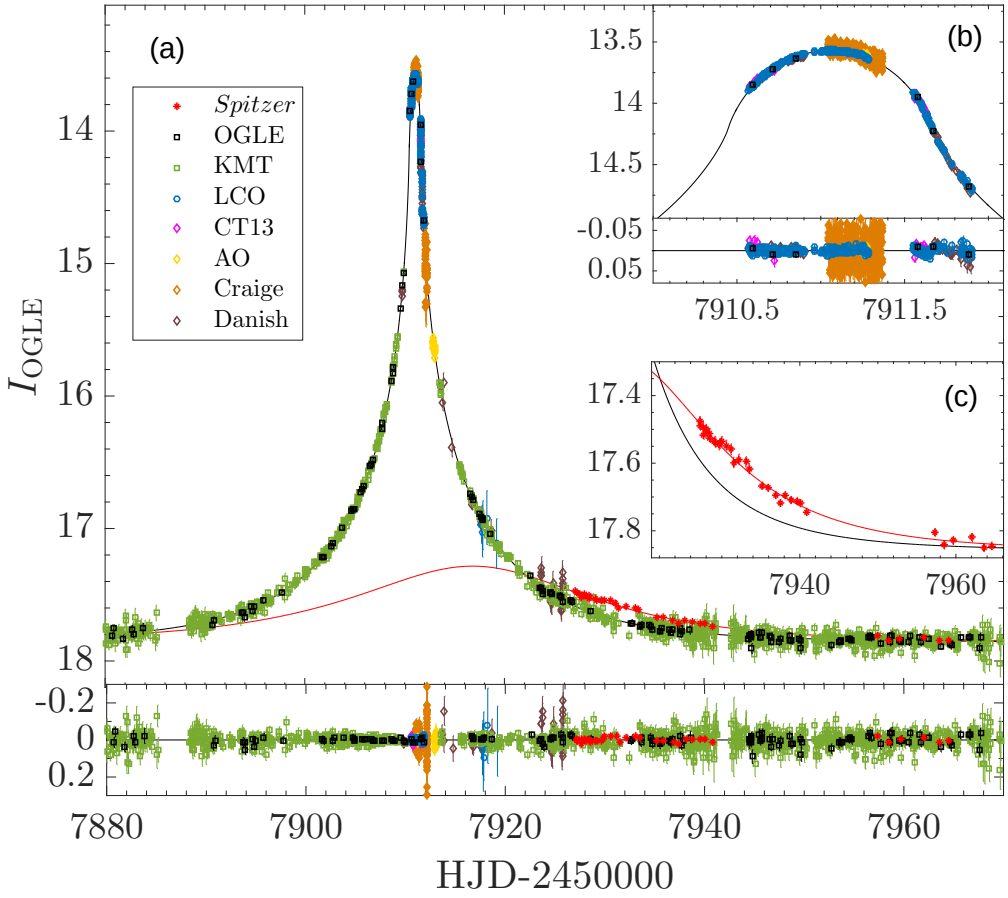

Figure 1. Light curve of OGLE-2017-BLG-0896. Finite-source effects are clearly seen at the peak of the event (inset b). The *Spitzer* light curve is significantly offset from the ground-based model (inset c), indicating the large microlens parallax.

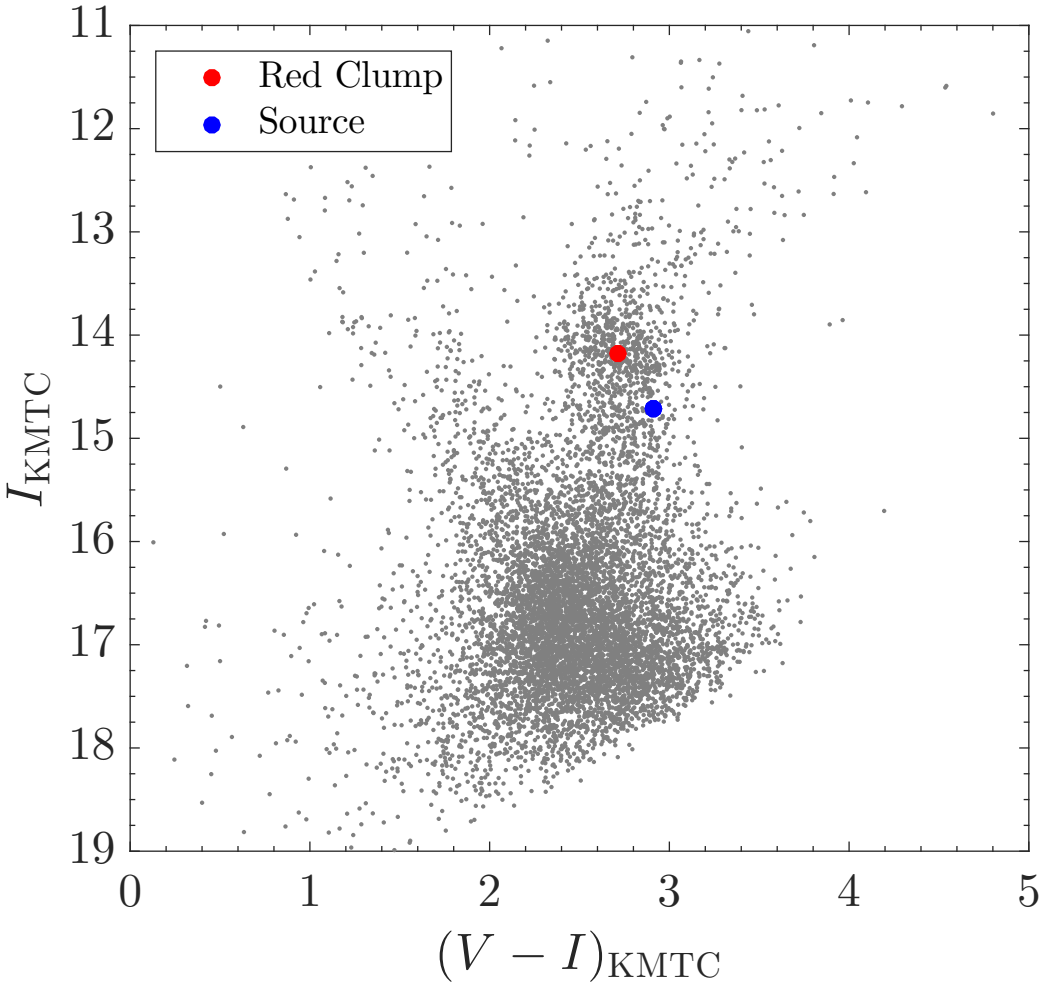

Figure 2. KMTC instrumental color-magnitude diagram of OGLE-2017-BLG-0896. The red clump (red) and source (blue) positions are marked.

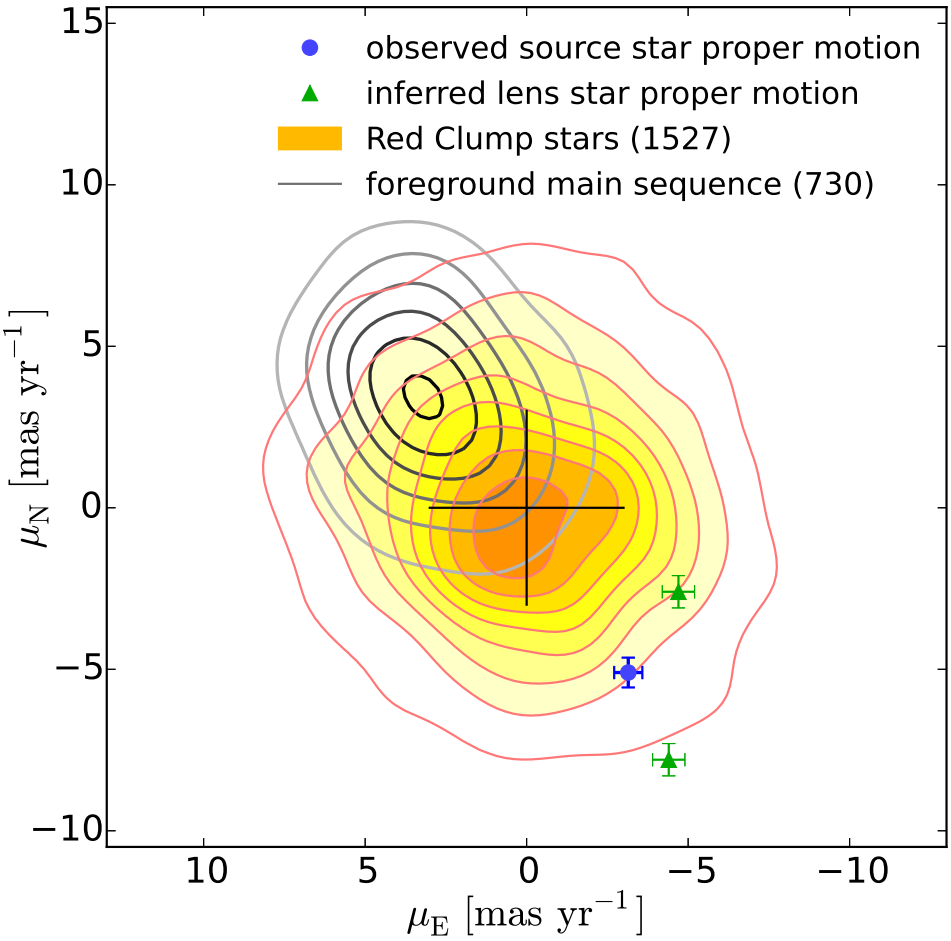

Figure 3. OGLE proper motion of bulge (red clump stars) and disk (foreground stars) populations. Approximately 95% of red clump stars are within the outer contour of the bulge proper-motion distribution, and ∼70% of foreground stars are within the outer contour of the disk proper-motion distribution. The source observed proper motion (blue circle) and the two degenerate solutions for the lens proper motion (green triangles) are shown.